Geophysical Journal International

Geophys. J. Int. (2022) **231,** 1421–1433
Advance Access publication 2022 July 1
GJI Seismology

https://doi.org/10.1093/gji/ggac254

Crustal and uppermost mantle structure of Cape Verde from ambient noise tomography

J. Carvalho [1], G. Silveira [1,2], S. Kiselev,[3] S. Custódio,[1] R. S. Ramalho,[1,4,5,6] E. Stutzmann[7] and M. Schimmel [8]

[1] *Instituto Dom Luiz (IDL), Faculdade de Ciências, Universidade de Lisboa, Campo Grande,* 1749-016, *Lisboa, Portugal. E-mail: jfcarvalho@fc.ul.pt*
[2] *Instituto Superior de Engenharia de Lisboa, Rua Conselheiro Emídio Navarro,* 1, 1959-007, *Lisboa, Portugal*
[3] *Institute of Physics of the Earth, Bolshaya Gruzinskaya str.,* 10-1 *Moscow* 123242, *Russia*
[4] *School of Earth and Environmental Sciences, Cardiff University, Park Place, Cardiff, CF*103*AT, UK*
[5] *Departamento de Geologia, Faculdade de Ciências, Universidade de Lisboa,* 1749-016 *Lisboa, Portugal*
[6] *Lamont-Doherty Earth Observatory, Columbia University, Comer Geochemistry Building, PO Box* 1000, *Palisades, NY* 10964-8000, *USA*
[7] *Institut de Physique du Globe de Paris, Université de Paris Cité, CNRS,* 1 *rue Jussieu,* 75005 *Paris, France*
[8] *CSIC, Geosciences Barcelona,* 08028 *Barcelona, Spain*

Accepted 2022 June 29. Received 2022 June 20; in original form 2021 September 24

SUMMARY

We present a seismic ambient noise tomography of the Cape Verde archipelago, located in the Atlantic Ocean, approximately 600 km west of Senegal. We used 38 seismic broad-band stations that continuously recorded for 10 months, in order to construct the first 3-D model of *Sv*-wave velocities for the crust and uppermost mantle beneath the Cape Verde region. We started by computing phase cross-correlations for vertical component recordings using all possible inter-island station pairs. Next, a time–frequency phase-weighted stack was applied to obtain robust Rayleigh-wave group-velocity dispersion curves in the period band between 10 and 24 s. Group-velocity maps at different periods are obtained by inverting the dispersion curves. We then inverted the group-velocity maps to obtain the 3-D shear wave velocity structure of the crust and uppermost mantle beneath Cape Verde. The final 3-D model extends from 8 km down to 23 km and has a lateral resolution of about 50 km. The crust in the southwestern sector, encompassing Fogo, presents lower *S*-wave velocities that may be caused by the presence of melt pockets and/or hydrothermal fluids circulation. The uppermost mantle beneath the northwestern sector is characterized by higher *S*-wave velocities in agreement with previous results obtained from *Ps* and *Sp* receiver functions. Those high-velocity anomalies can reflect non-altered crust or remnants of magma chambers or solidified basaltic intrusions, which fed the volcanism in these islands. Our maps revealed the presence of crustal underplating across the entire archipelago, yet stronger beneath the groups Santo Antão—São Vicente—São Nicolau and Fogo—Santiago—Maio.

Key words: Seismic noise; Seismic tomography; Surface waves and free oscillations; Crustal structure; Oceanic hotspots and intraplate volcanism.

1 INTRODUCTION

The relatively simple structure of the oceanic crust and suboceanic uppermost mantle, although dependent on age and drifting speed, becomes highly complex in the vicinity of within-plate volcanic regions (e.g. Leahy *et al.* 2010; Gorbatikov *et al.* 2013; Fontaine *et al.* 2015). The Cape Verde Archipelago, which has been formed over a hotspot, is no exception and is assumed to be more complex than its surroundings, attracting much interest. Moreover, Cape Verde is considered an example of a stationary volcanic archipelago with respect to its melting source (McNutt 1988), and so presumably its deep structure may reflect the effects of cumulative intrusive and magmatic processes, over an inferred 26 Ma lifetime of the hotspot.

Accurate 3-D models of the seismic structure beneath hotspots are of extreme importance to understand the mantle to surface mass transfer, as well as the lithospheric tectonic evolution, and further contributing to a better location of local earthquakes and seismic and volcanic hazard assessment. Several seismic studies have contributed to illuminating Cape Verde's deeper seismic structure (e.g. Helffrich *et al.* 2010; Vinnik *et al.* 2012; Carvalho *et al.* 2019b; Liu & Zhao 2021). However, given the geometry of the seismic networks in the archipelago and the irregular distribution of the

seismic events (Faria & Fonseca 2014; Vales *et al.* 2014), crustal and uppermost mantle studies have been limited to 1-D profiles beneath some of the islands (Lodge & Helffrich 2006) or 2-D seismic profiles across the entire Cape Verde Archipelago (e.g. Ali *et al.* 2003; Pim *et al.* 2008; Wilson *et al.* 2010, 2013). Our motivation is to investigate the structure of the crust and uppermost mantle beneath Cape Verde, generating a 3-D shear wave velocity model of the region.

Local earthquake tomography and controlled-source seismology are the methods most used to investigate the seismic structures of the crust and uppermost mantle. Nevertheless, the inadequate source–receiver geometry across Cape Verde does not allow local earthquake tomography and active-source seismology is extremely expensive.

For long, ambient seismic noise was considered a nuisance to be discarded from seismograms, obscuring seismic information in earthquake signals. However, nowadays, ambient noise is one of the fastest-growing fields in the Earth sciences and is widely applied for different purposes [e.g. hydrocarbon exploration (Bussat & Kugler 2009); geological engineering (Picozzi *et al.* 2009); fluid injection monitoring (Stork *et al.* 2018), volcanism (Wang *et al.* 2017) or fault mapping (Brandmayr *et al.* 2016)]. Ambient seismic wavefield recordings are predominantly dominated by surface waves and can be widely recorded at periods which are suitable to image the Earth's crust and upper mantle. These surface waves can be obtained by seismic interferometry and then analysed by ambient noise tomography (ANT).

In the last decades, ANT has been successfully applied worldwide, at different scales: Regional scales, such as in the western United States (e.g. Shapiro *et al.* 2005; Moschetti *et al.* 2007), Madeira Island (Matos *et al.* 2015), West of Java, Indonesia (Pranata *et al.* 2019) or Costa Rica (Nuñez *et al.* 2019); continental scales such as Europe (Yang *et al.* 2007; Lu *et al.* 2018), North America (Bensen *et al.* 2008) and Australia (Saygin & Kennett 2012) and even at global scales (e.g. Nishida *et al.* 2009; Haned *et al.* 2016).

In this study, we analyse continuous seismic data from a total of 38 broad-band stations, temporarily deployed across the Cape Verde Islands (Weber *et al.* 2007, Fig. 1b). Station pairs located on the same island were discarded due to the small inter-station distances. In total, we extracted empirical Green's functions (EGFs) from 6-hr long cross-correlations of the vertical component at 634 station pairs. We applied a phase cross-correlation (PCC) processing technique, followed by a time–frequency Phase Weighted Stack (tf-PWS) developed by Schimmel *et al.* (2011). Inter-station group-velocity measurements obtained by *S* transform (Schimmel *et al.* 2017) were then inverted to infer lateral perturbations of the group velocities through the fast marching surface tomography (FMST) method (Rawlinson & Sambridge 2005). From these we obtained a 3-D shear wave velocity model, constraining the solid Earth structure from 8 km down to 23 km depth.

2 GEODYNAMIC SETTING

The volcanic Cape Verde Archipelago is composed of ten islands located in the eastern Atlantic Ocean [14°–18° N and 22°–26° W], 600–850 km off Senegal coast, West Africa (Fig. 1a). The islands are arranged in a west-facing horseshoe shape, with two diverging chains. The non-existence of a linear track with a time–distance correlation between islands has been interpreted as a result of the closeness between the rotation pole for the Nubian plate and the archipelago (Burke & Wilson 1972; Pollitz 1991), which is thus considered nearly stationary over the melting source that fed the islands' volcanism (McNutt 1988; Lodge & Helffrich 2006; Holm *et al.* 2008; Ramalho *et al.* 2010a). The islands rest on top of one of the largest bathymetric anomalies in the Earth's oceans—the Cape Verde Rise—which is considered a hotspot swell (e.g. Sleep 1990; Pim *et al.* 2008; Wilson *et al.* 2010) thermally rejuvenated down to an age of 59 Ma (Sleep 1990) or even to 30 Ma (Carvalho *et al.* 2019b).

Magnetic anomalies and bathymetric data suggest that the islands are placed on an ∼80 km thick, old oceanic lithosphere (120–140 Ma; Müller *et al.* 2008). Pim *et al.* (2008) proposed a regional oceanic crust of ∼7–13 km thickness beneath the Cape Verde swell. These values were later corroborated by Wilson *et al.* (2010, 2013), based on seismic and gravimetric constraints. However, under the individual islands, the crust appears to be thicker (10–22 km), as suggested by the analysis of *Ps* receiver functions by Lodge & Helffrich (2006). Later, Vinnik *et al.* (2012), using a joint inversion of *Ps* and *Sp* receiver functions for three different groups of islands, suggested an even thicker crust (10–30 km), which they interpreted as due to the presence of a magmatic underplate layer. Recently, Liu & Zhao (2021) presented a 1-D V_S model, indicating a Moho depth across all archipelago at approximately 15 ± 10 km.

Exposed volcanism in Cape Verde Archipelago dates to the Oligocene (25.6 ± 1.1 Ma) and extends well into the Holocene (Torres *et al.* 2010). Historical eruptions (i.e. < 500 yr) are unknown, except on Fogo, where the last eruption occurred in 2014/2015 (Mata *et al.* 2017, and references therein). A faint age progression can be observed along the eastern-to-southern chain, which agrees simultaneously with the age of the oldest exposed volcanic sequences, by the age progression of the shield phase, both with ages decreasing towards the southwest, and with the progressively younger volcanic morphology and relief of the islands towards the west (e.g Ramalho 2011; Samrock *et al.* 2019).

Seismicity in the archipelago is sparse, detected essentially in the islands of Fogo, Brava and Santo Antão, as well as offshore, typically related to volcano-tectonic activity and to active seamounts or submarine cone fields (e.g. Grevemeyer *et al.* 2010; Faria & Fonseca 2014; Leva *et al.* 2019). Vales *et al.* (2014), using the same seismic network as in this study, analysed the seismicity of the region, and confirmed that most earthquakes are concentrated in the westernmost areas of the archipelago (Fig. 1b).

3 DATA AND EMPIRICAL GREEN FUNCTIONS

We processed continuous seismic waveform data from 38 temporary stations of the 9A network (Weber *et al.* 2007, Fig. 1b). These stations were equipped with Earth Data PR6-24 data loggers and Guralp CMG-3ESP seismometers and recorded during 10 months from 2007 December until 2008 September, with a sampling rate of 100 Hz. Inter-station distances vary from ∼22.5 to ∼295 km, not counting stations on the same island.

For each station, continuous vertical-component seismic data were cut into 6-hr length segments. The corresponding 6-hr time-series were downsampled from the original 100 to 2 Hz, demeaned and detrended. The instrument response was removed in order to obtain ground velocities and the seismograms were then bandpass filtered in the 0.03–0.5 Hz frequency band.

The subsurface properties between two seismic receivers are expressed by Green's functions. To determine the EGFs we applied the PCC, followed by the tf-PWS, as proposed by Schimmel *et al.*

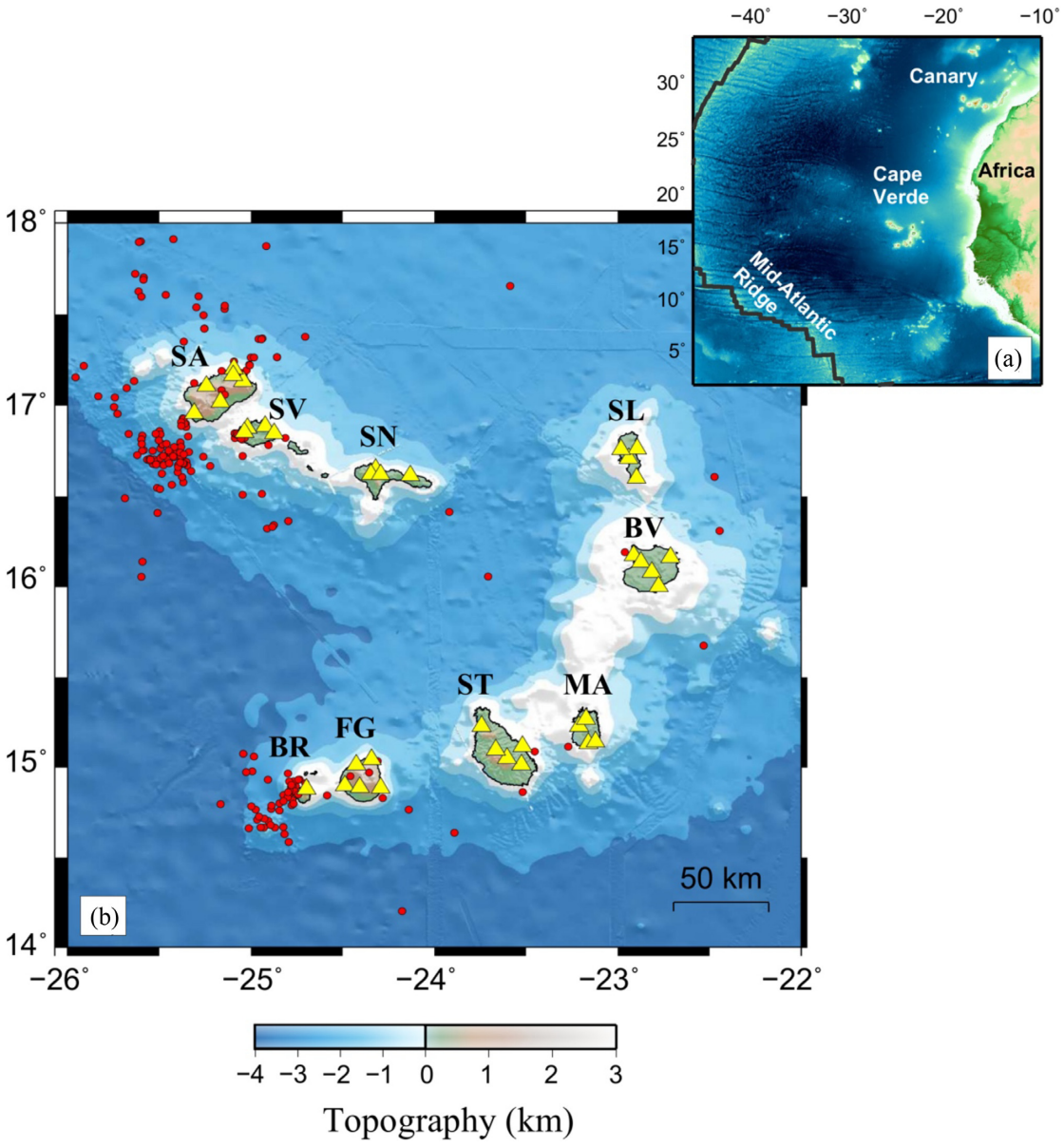

Figure 1. (a) Topographic map of the Central Atlantic region. (b) Geographic distribution of the islands, bathymetry of the archipelago (GEBCO Compilation Group 2020) and abbreviated names of the islands: SA—Santo Antão; SV—São Vicente; SN—São Nicolau; SL—Sal; BV—Boavista; MA—Maio; ST—Santiago; FG—Fogo and BR—Brava. Triangles in yellow represent the 9A seismic network (Weber *et al.* 2007), encompassing 38 stations, whereas the red circles represent the seismicity between 2007 and 2008 detected by Vales *et al.* (2014), for depths ranging between 0 and 30 km.

(2011). PCC is amplitude unbiased and therefore does not require time-domain normalization or spectral whitening in order to remove unwanted signals or to reduce the effect of high energy signals such as earthquakes (Schimmel 1999; Schimmel *et al.* 2011).

PCC were calculated for 634 inter-station pairs, for time lags between −300 and 300, which includes the surface wave train at the longest inter-station distances. Instead of the traditional linear stacking procedure, we then applied the tf-PWS stacking of Schimmel *et al.* (2011). Previous studies jointly applied the PCC and the tf-PWS methods and demonstrated that they result in improved signals and more robust group-velocity measurements (e.g. Haned *et al.* 2016; Corela *et al.* 2017; Poveda *et al.* 2018; Acevedo *et al.* 2019; Hable *et al.* 2019; Nuñez *et al.* 2019). For more details on these methods the reader is referred to Schimmel & Gallart (2007) and to Schimmel *et al.* (2011).

Inter-station paths and corresponding EGFs sorted by their inter-station distance are shown in Figs 2(a) and (b). EGFs were constructed by stacking both the causal and acausal segments for each station pair, after time-reversing the acausal part. Some asymmetries can be observed on EFGs, which is a consequence of the heterogeneous distribution of the seismic noise sources (Carvalho *et al.* 2019a).

Since we are working with the *ZZ* components (i.e. cross-correlations between vertical-component seismograms), we expect EGFs to consist mainly of Rayleigh waves. Indeed, Fig. 2 shows prominent wave arrivals corresponding to the expected propagation velocities, between 1.8–3.6 km s^{-1}. A second slower arrival is also visible, with velocities ranging between 1.0–1.3 km s^{-1}. This second wave train is mainly detected in the EGFs corresponding to station pairs separated by deep ocean. Other authors have previously

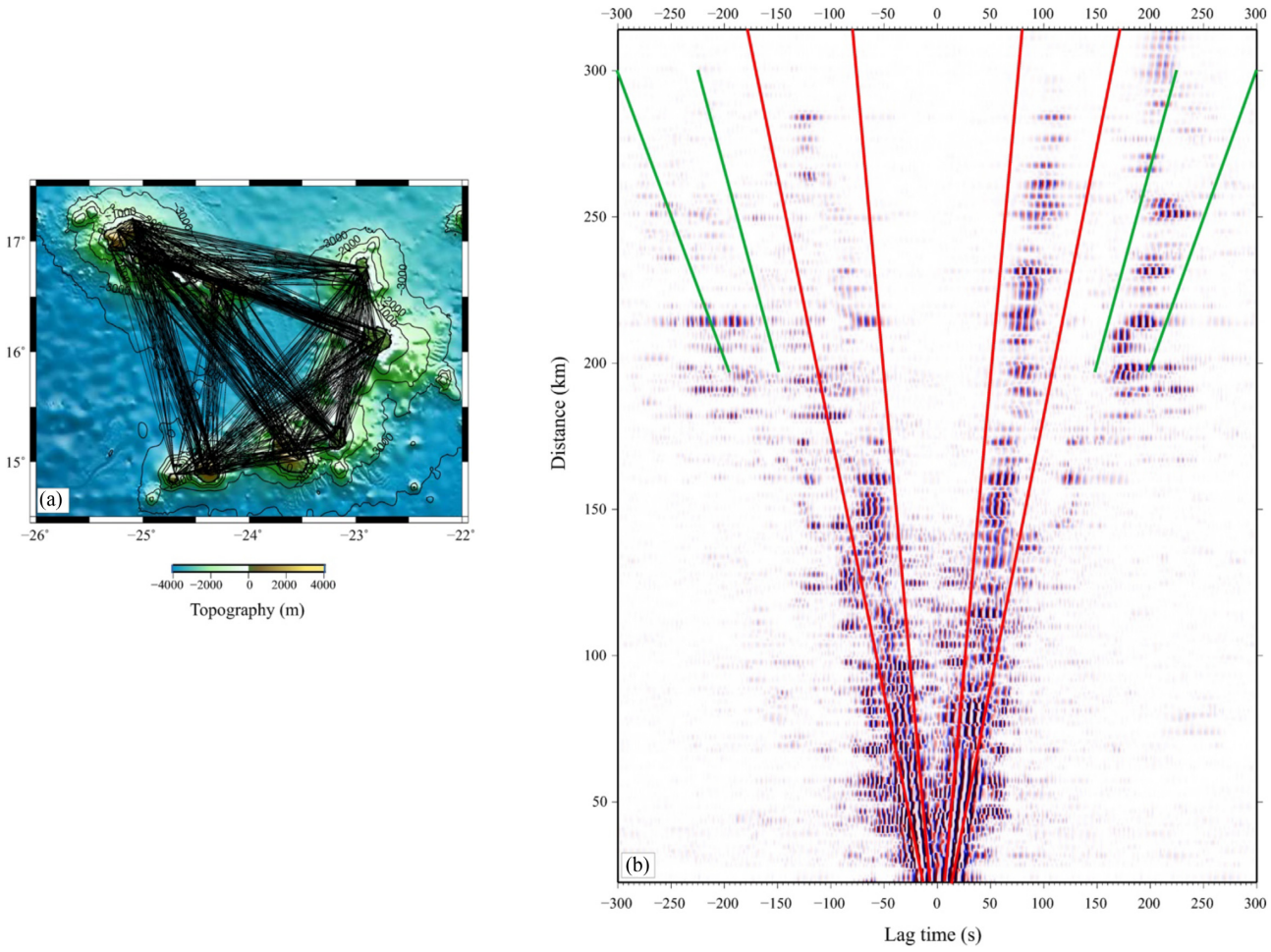

Figure 2. (a) Inter-station paths corresponding to the 634 station pairs for which EGFs were computed. (b) EGFs sorted by inter-station distance. The red lines delimit the Rayleigh wave arrivals, with velocities between 1.8–3.6 km s^{-1}. A slower arrival is also seen bounded by green lines, with velocities between 1.0–1.3 km s^{-1}.

detected such a second wave package with significantly lower velocity in oceanic environments on EGF measured between ocean–bottom seismometers (OBS, e.g. Le *et al.* 2018; Hable *et al.* 2019).

4 AMBIENT SEISMIC NOISE GROUP-VELOCITY MEASUREMENTS

In order to measure group-velocity dispersion curves, we applied the strategy developed by Schimmel *et al.* (2017), for a robust and semi-automated estimation of group velocities from energy diagrams, based on the *S* transform and using a resampling approach. The *S* transform uses frequency-dependent scaling windows in comparison to the wavelet transform, overcoming some of its disadvantages (Stockwell *et al.* 1996). It has proven to be a powerful tool to transform the EGF in the time–frequency domain.

For extracting group-velocity values that can be associated with Rayleigh waves, we defined a velocity range of 1.5–4.5 km s^{-1} for Rayleigh wave measurements, based on the record section of Fig. 2. We also selected a frequency range of 0.03–0.5 Hz (T ∼2–30 s). Fig. 3 shows an example of the group-velocity measurements calculated for the inter-station path CVBV1–CVSA4. The same procedure was applied to all possible station pairs, with the exception, of those located on the same island, as mentioned before. In most of the energy diagrams we observed that amplitudes are very high for a broad range of group velocities at high frequencies (above 0.1 Hz), thus the automated procedure has some difficulty in selecting single dispersion measurement in this range (Fig. 3).

In Fig. 3, we can observe that the code automatically selects a few measurements at higher frequencies (which seem to be an overtone) but because the next measurements to be considered exhibit much lower velocities, they are not accounted. The code is prepared to avoid these oscillations. Thus, the next signals to be considered are the ones below 0.1 Hz, where there is only one clear measurement. Despite the detection of black dots (maxima) in the entire frequency band, the presence of multiple signals, especially at higher frequencies (above 0.1 Hz), prevents the code from correctly selecting a dispersion curve for these. In several other measurements, even when an energy-dominant signal fits the established parameters, the code selected what seems to be overtones (Fig. S1.1, Supporting Information). To overcome this problem, we tested the approach of Haned *et al.* (2016), later also followed by Hable *et al.* (2019), and filtered each trace into three narrower frequency bands (0.03–0.1, 0.1–0.2 and 0.2–0.5 Hz). However, this procedure did not improve significantly our group-velocity measurements (Fig. S1.2, Supporting Information) as it did not allow to follow a continuous group velocity as a function of frequency. All the dispersion curves were finally quality checked manually, so that we kept only dispersion curves free of ambiguity. Fig. 4 shows all the selected dispersion

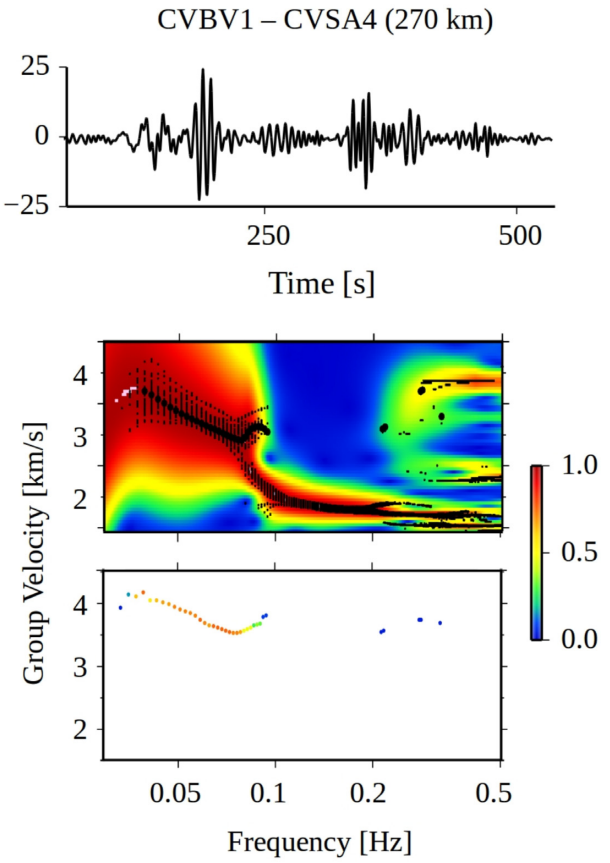

Figure 3. EGFs obtained in the frequency band 0.03–0.5 Hz for the inter-station path CVBV1–CVSA4 (270 km long; top panel), the corresponding energy diagram (middle panel) where the black dots mark all the detected maxima, and the selected dispersion curve (bottom panel).

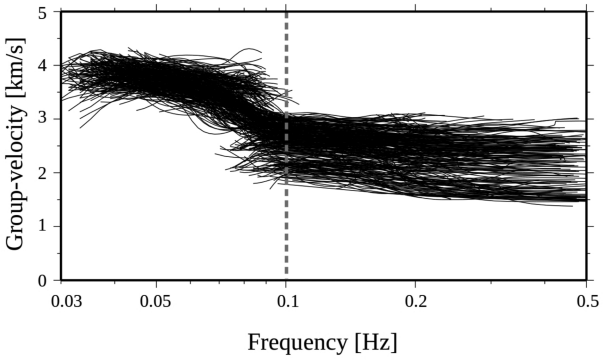

Figure 4. Measured dispersion curves for all possible inter-station paths (after removal of outliers). The dashed grey line separates the curves discarded (above 0.1 Hz) from the ones used in the tomography (below 0.1 Hz).

curves. In general, the measured dispersion curves are consistent with each other, clustering into a single group. Most dispersion measurements exhibit rapidly changing velocities at ∼0.1 Hz and multiple dispersion branches, probably overtones, making impossible to follow the fundamental-mode group velocity as a function of frequency. This same behaviour was found in other studies where paths cross both water and land (Corela *et al.* 2017) or a larger water portion compared to the land portion (Hable *et al.* 2019; Schlaphorst *et al.* 2021). This feature seems to be characteristic of oceanic environments and both Hable *et al.* (2019) and Schlaphorst *et al.* (2021) discarded all dispersion measurements for frequencies higher than 0.1 Hz.

Considering the detected multiple signals in most energy diagrams above 0.1 Hz, and the automatically selected dispersion curves (Fig. 3), we modelled Rayleigh-wave fundamental-mode synthetics in a laterally varying medium to verify if the fundamental mode was properly isolated from the overtones (Herrmann 2013). This analysis (see Supporting Information for detailed explanation) shows not only that the fundamental mode is not clearly separated from higher modes but also that the water layer has a clear influence on high-frequency ($>$ 0.1 Hz) Rayleigh wave dispersion measurements.

In the Cape Verde area, the ocean has a depth of 3–4 km between some islands. According to our synthetic group-velocity dispersion curves (see Fig. S2.2, Supporting Information), we then expect that for frequencies higher than 0.1 Hz the fundamental mode is not clearly separated from the higher modes. Thus, Rayleigh-wave group-velocity dispersion curves for frequencies above 0.1 Hz will not be considered in our tomographic computations. In future work, we intend to investigate the feasibility of using Love waves in order to improve the resolution of our models and eventually image the structure below the current 23 km depth. In fact, it is important to take into consideration the Love waves in ANT of oceanic environments, since these waves are not affected by the water layer (Pinzon *et al.* 2019).

5 TOMOGRAPHY

To obtain a 3-D model of *S*-wave velocity we followed a commonly applied surface wave tomography two-step approach. In the first step, we computed maps with the lateral variation of group velocity, as a function of period, using the FMST method of Rawlinson & Sambridge (2005); in the second step, we inverted the group-velocity maps by using a trans-dimensional inversion technique to obtain the local *S*-wave velocity at each gridpoint as a function of depth (Haned *et al.* 2016; Silveira *et al.* 2022).

5.1 Group-velocity maps

FMST is a nonlinear tomographic inversion suitable to determine group-velocity maps for different periods that relies on two steps: (1) prediction of traveltimes (forward problem) and (2) adjustment of the model parameters that best match the data, using regularization constrains (inverse problem).

The 2-D model of group velocities for each period is parametrized with 150 velocity nodes, over a grid spaced 0.4° in latitude × 0.3° in longitude, which constitute the inversion grid. A constant initial velocity was taken from the average group-velocity dispersion curve to initialize the inversion. Several synthetic checkerboard tests were performed, with different grids spacings, in order to decide the final grid dimension and thus to estimate the maximum available resolution with the current network design (Fig. S3, Supporting Information). Fig. 5 shows the input synthetic checkerboard group-velocity map, with the final grid-cell size, as well as the recovered anomalies for $T \sim 11$, 17 and 20 s, for the chosen grid spacing and regularization parameters. Despite the challenging distribution of the network, which results from the distribution of the islands in a horse-shoe shape and from the lack of OBSs to fill the oceanic gaps, the resolution tests indicate that a well-resolved velocity model for the considered period range (10–24 s) can be obtained. The number of inter-station paths is similar for all selected periods, which results

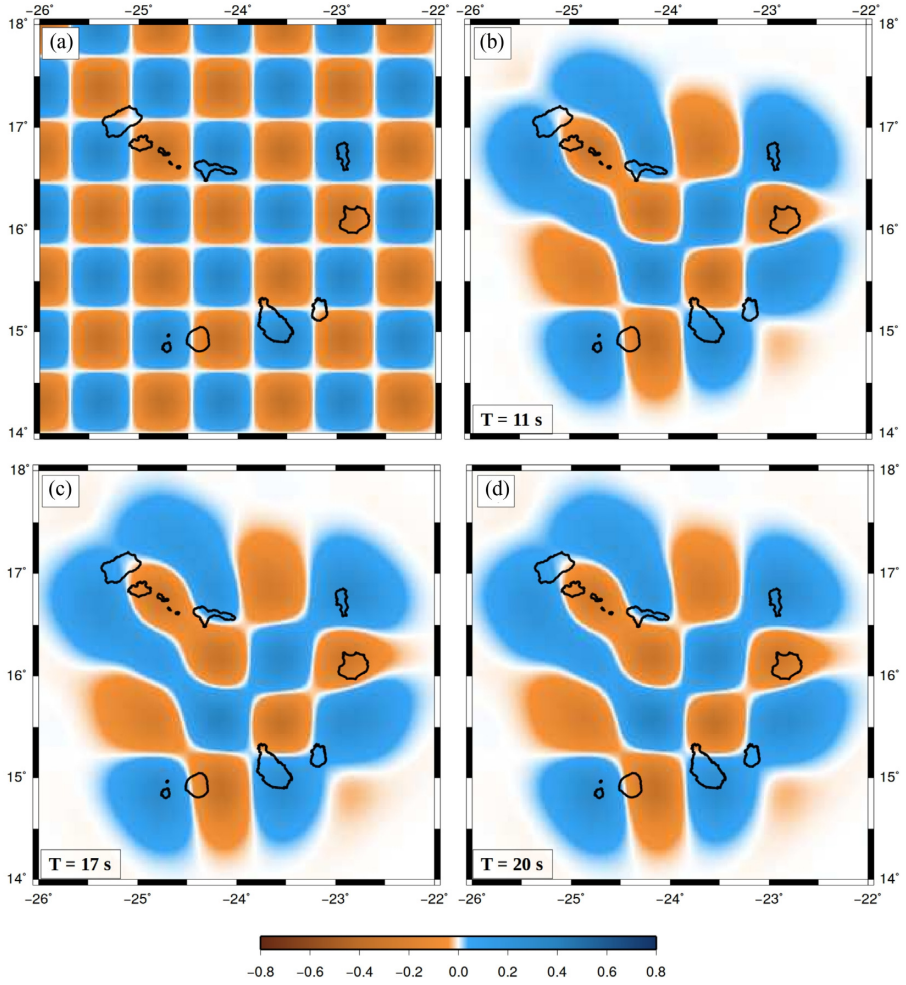

Figure 5. Synthetic input checkerboard [panel a)] and the recovered output anomalies for $T = 11$, 17 and 20 s [panels (b), (c) and (d), respectively].

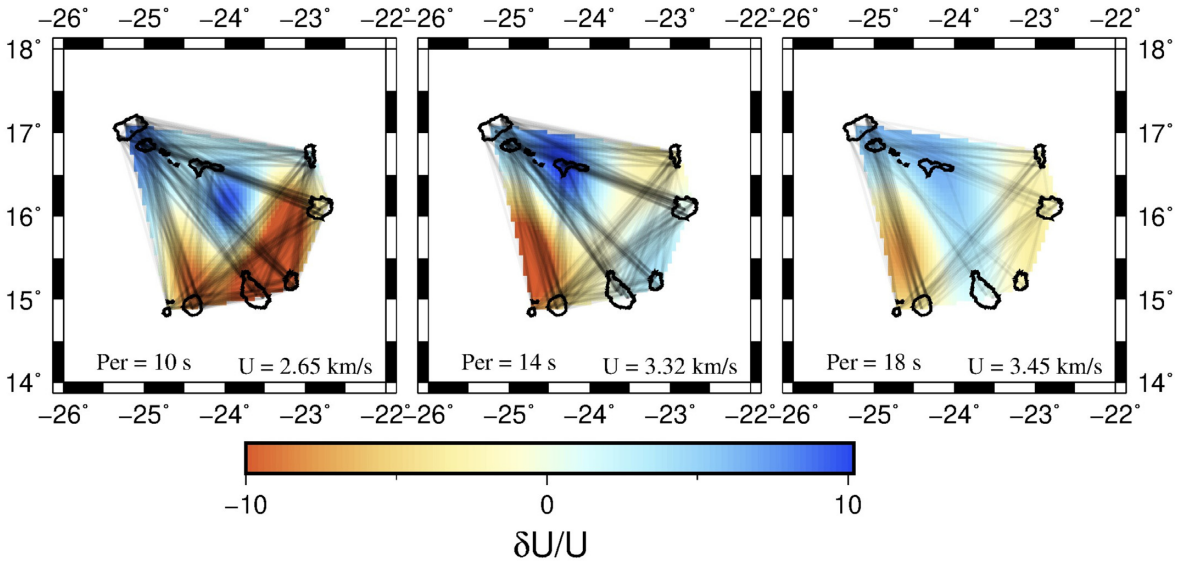

Figure 6. Rayleigh-wave group-velocity maps for selected periods of 10, 14 and 18 s. Black lines represent the inter-station paths used for each period.

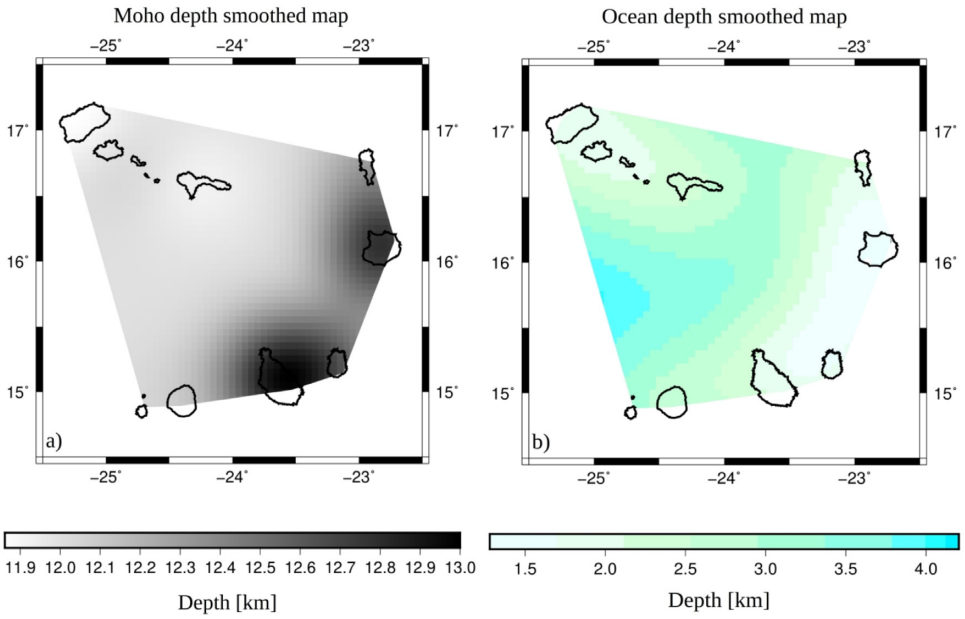

Figure 7. (a) Map of smoothed Moho depth showing that Moho depths vary in a narrow range between 11.9 and 13 km. (b) Smoothed bathymetric map displaying the existence of a water layer in the *a priori* model, even in the islands.

in similar resolution at all periods. Measurements for inter-station distances shorter than two wavelengths were discarded as they tend to represent poorly the sampled structure.

The regularization parameters applied to stabilize the inversion, smoothing (η) and damping (ε), were chosen after repeated iterations, for different values of damping and smoothing, as in Rawlinson *et al.* (2006). We varied the damping factor from 0.5 to 50 and determined that $\varepsilon = 5$ represents a good compromise between data misfit (RMS) and model variance. The same procedure was applied to determine the smoothing parameter. We now varied the smoothing from 1 to 750, after fixing the damping parameter at 5. A good compromise between data misfit (RMS) and model roughness was found for $\eta = 50$. In general, the impact of these parameters on the inversion result was rather low. The L-shaped trade-off curves in Fig. S4 (Supporting Information) represent the variation of the RMS data misfit as a function of model roughness, model variation and number of iterations in those tests. For the chosen parameters, $\varepsilon = 5$ and $\eta = 50$, the inversion converges quickly after three iterations (Fig. S4, Supporting Information).

Fig. 6 presents our final group-velocity maps for periods of 10, 14 and 18 s, as well as the corresponding ray coverage. Slower and faster than average velocities are presented with warmer and cooler colours, respectively. Complete results for all periods are available in the supporting information (Fig. S5, Supporting Information).

The group-velocity maps display higher velocities in the north-western group of islands, for the entire period band. In opposition, the islands of Fogo and Brava exhibit lower velocities at all periods.

5.2 *S*-wave velocity model

Next, the group-velocity maps were inverted to obtain the tomographic *S*-wave velocity model as described in Haned *et al.* (2016) and Silveira *et al.* (2022). The inversion performed here is identical to the one applied in Silveira *et al.* (2022). For this study a water layer was included on the *a priori* model and the group-velocity measurements were only considered below 0.1 Hz.

The inversion is computed for each point of a grid of 0.05° × 0.05° in latitude and longitude. At each gridpoint, synthetic group velocities are computed for different periods assuming a given *S*-wave velocity model, as a function of depth.

The inverse problem is non-unique unless a smoothing condition is imposed on the trial *S*-wave velocity model. The Moho discontinuity must also be considered. To integrate both conditions, the *S*-wave velocity model is represented as the sum of the *a priori* model with discontinuities plus a continuous and smoothed curve expressed as a series of B-spline basis functions with weight coefficients, which are the model parameters. The absence of shorter periods is handled by the inversion code using a higher level of regularization (i.e. the inverse of the number of splines).

In Haned *et al.* (2016), the crustal model was taken from crust1.0 (Laske *et al.* 2013) to obtain their tomographic model. Here, as we work at a small scale and in an oceanic environment, we determine a uniform *a priori S*-wave velocity in the crust. Our *a priori* model consists of a water layer and an uniform layer for the crustal part followed by the PREM (Dziewonski & Anderson 1981) for the mantle.

In our *a priori* model, the Moho depth is given by Lodge & Helffrich (2006) for the islands and Pim *et al.* (2008) for the oceanic basin. Due to the wavelength of surface waves, which does not allow the resolution of small-scale changes in Moho depth, we smoothed the depth lateral variations of the Moho, with a correlation length $L_{cor} = 50$ km.

After smoothing, Moho depths vary in the narrow range from 11.9 to 13 km (Fig. 7a), showing that the oceanic Moho depth dominates due to the small size of the islands. Following the same approach, in order to compute the water layer, the bathymetric map of the region was also smoothed (Fig. 7b). We can see that after smoothing the *a priori* model has a water layer even in the islands.

Sensitivity kernels indicate that the Rayleigh wave group velocities are mostly sensitive to structure down to about 30 km (Fig. S6, Supporting Information). Therefore, we consider that our *S*-wave

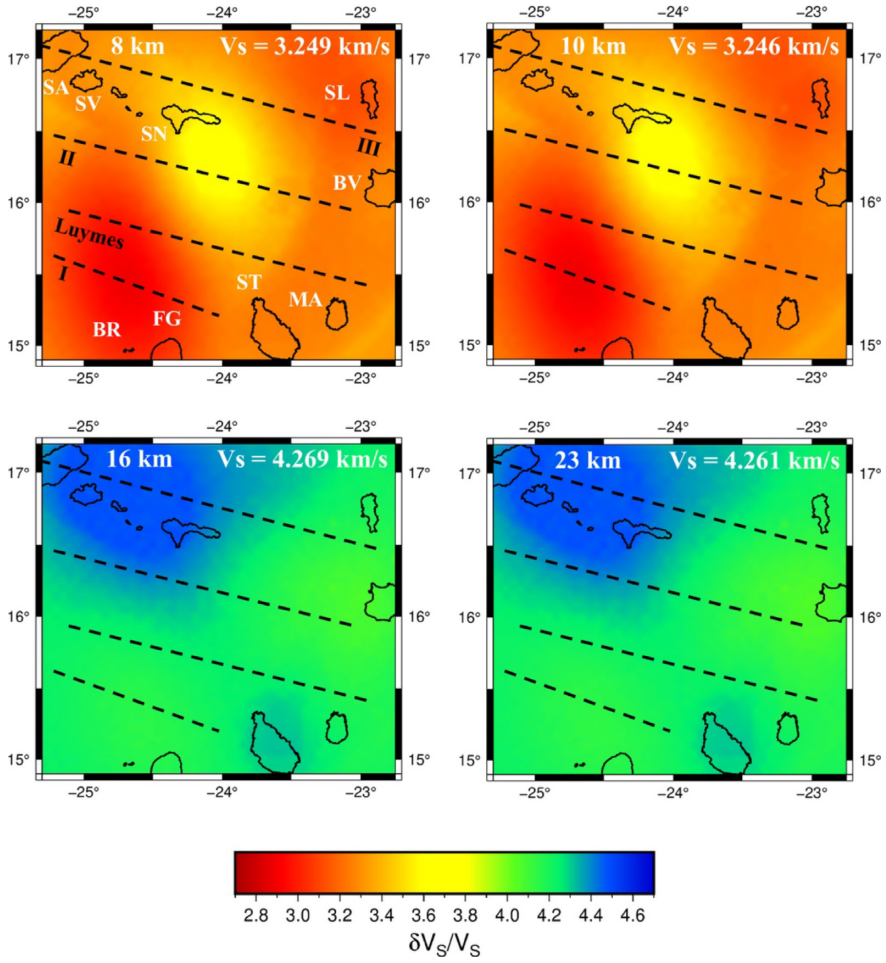

Figure 8. *S*-wave velocity models at different depths resulting from the inversion of group-velocity maps. Velocities are plotted as absolute values. The depth and laterally averaged *S*-wave velocities are indicated at the top of each map. Velocity variations range from 2.7 to 4.7 km s^{-1}. Dashed lines represent the fracture zones proposed by Williams *et al.* (1990). We included their names on the top left map, as well as the abbreviated names of the islands: SA—Santo Antão; SV—São Vicente; SN—São Nicolau; SL—Sal; BV—Boavista; MA—Maio; ST—Santiago; FG—Fogo and BR—Brava.

model can be interpreted until a depth of approximately 30 km, which contains information on the crust and uppermost mantle structure.

Fig. 8 presents the tomography slices at different depths. Each plot shows the distribution of *S*-wave velocities at selected depths in percentage with respect to the average velocity value at each depth. The average *S*-wave velocity value is plotted on the top-right corner of each slice, for reference.

At most depths the velocity exhibits smooth variations, as would be expected from a surface wave tomography. In the top 10 km, our model displays lower velocities beneath the islands and between Fogo and Santo Antão. The lowest values occur in the area beneath Brava and Fogo. From 10 km down to 23 km, the velocities increase in all the studied area, however the area beneath the northwestern islands exhibits a clear higher velocity, which seems to have some expression also beneath Santiago. The areas beneath the remaining islands show velocities close to the average. These anomalies are consistent down to the limit of our model (∼ 23 km depth).

Fig. 9 presents several vertical profiles that extend from 8 km down to 18 km (with vertical exaggeration). These cross sections show low shear wave velocities from approximately 8 to 13 km depth consistently in all the archipelago. However, as already observed in Fig. 8, the velocities are lower surrounding the island of Fogo and higher close to São Nicolau. At approximately 12–14 km depth, we detect the presence of a lenticular shaped higher velocity. Deeper, and as already observed in Fig. 8, most of the velocities become close to the average shear wave velocity, with exception of the group of Santo Antão—São Vicente—São Nicolau, which exhibits higher velocities.

6 DISCUSSION

Our 3-D shear wave velocity model offers new insights on the structure beneath Cape Verde at crustal and uppermost mantle depths, contributing with important information on the upper structure of this region (8 to ∼23 km). At shallow depths (< 12 km) the islands are characterized, in general, by lower velocities than those of the oceanic area between São Nicolau and Santiago. At those depths, the lowest velocities are found to the north–northwest of Fogo, between fracture zones I, Luymes and II, as can be seen in Fig 9i). Fogo and Brava are the youngest and (presently) most active volcanoes in the archipelago. For the top few km (∼ 12 km), corresponding to the crust, the low-velocity anomaly in this region may be the result of a much higher predominance of melt pockets, in

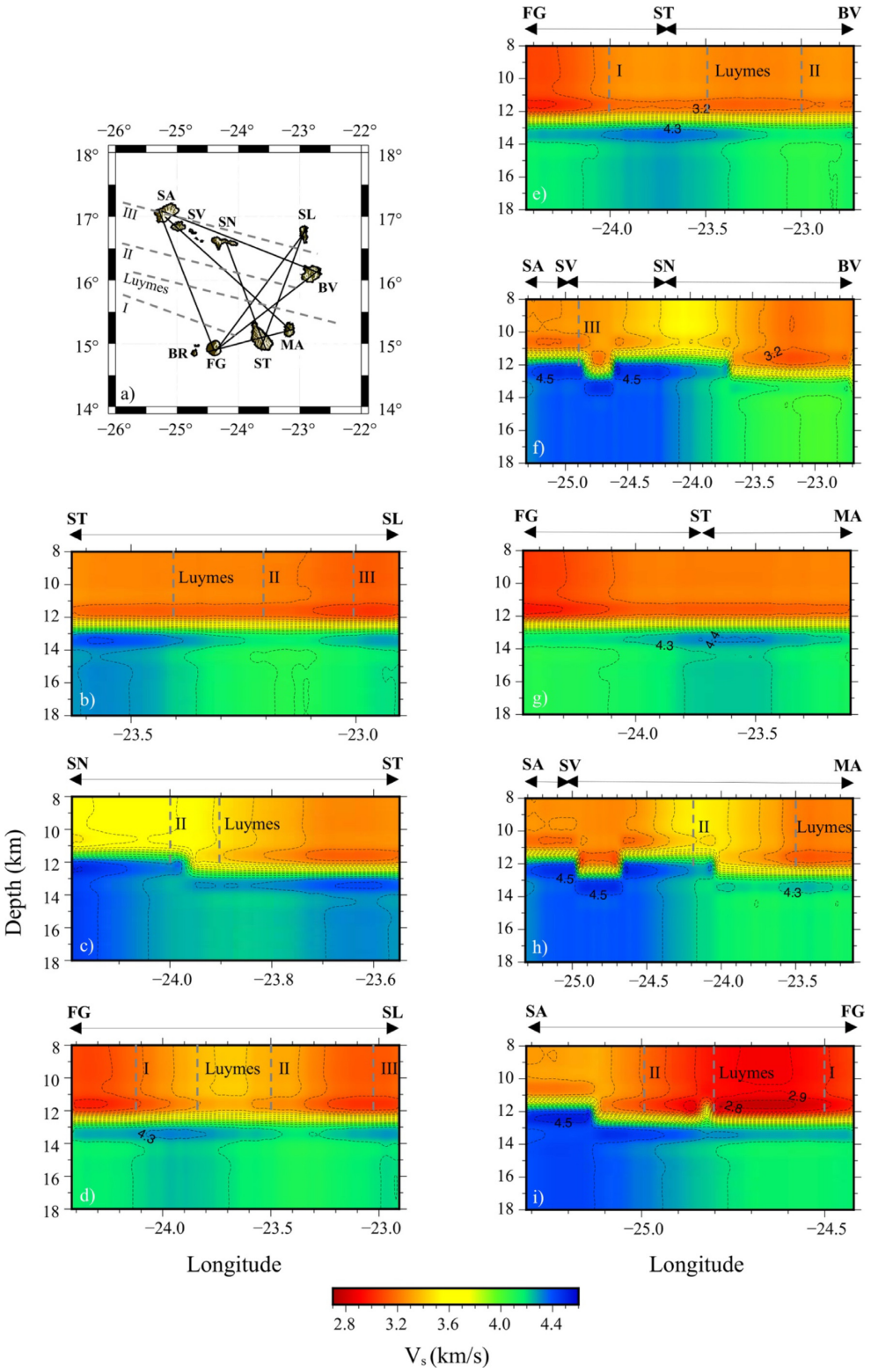

Figure 9. (a) Simplified topographic map of Cape Verde showing the selected profiles, the abbreviated names of the islands and the fracture zones (dashed lines) published in Williams *et al.* (1990). (b)–(i) Vertical profiles through the 3-D shear wave velocities, represented in absolute velocities. Vertical dashed lines show the fracture zones identified in (a).

good agreement with the active volcanism observed in this part of the archipelago. Fogo and Brava also exhibit the thinnest crust (e.g. Lodge & Helffrich 2006; Vinnik *et al.* 2012) and are the sites of ongoing intrusive processes at crustal and uppermost mantle levels, as demonstrated by the recorded seismicity and recent volcanism (see Faria & Fonseca 2014; Vales *et al.* 2014; Leva *et al.* 2019). These characteristics suggest a hotter, melt-rich crust and uppermost mantle beneath and in the vicinities of these islands, in contrast with the

rest of the archipelago, where crustal seismic velocities are higher. The extension of this anomaly further to the north is somewhat enigmatic, but it may suggest that melt pockets—or recent intrusions—at shallower levels are more widespread than previously thought. It is worth mentioning that the northwest terminus of the archipelago was also the site of recent vigorous volcanism and exhibits recorded seismicity attesting to volcanic unrest and consequently active volcanism (Faria & Fonseca 2014; Vales *et al.* 2014; Eisele *et al.* 2015); intriguingly, however, the lower shear wave velocities do not fully extend to the northwest terminus of the archipelago. As such, the observed shear wave velocity reduction could also eventually be explained by more intense hydrothermal alteration of the oceanic crust in this area, leading to a reduction in shear wave velocities.

The analysis of compressional to shear (*P* to *S*) converted seismic phases by Lodge & Helffrich (2006) pointed to a Moho discontinuity shallower beneath the Santo Antão and São Nicolau, and deeper beneath the remaining islands. Although neither the Moho depth nor the *Vs* velocity discontinuity at Moho depth are resolvable by surface waves, the distribution of the *S*-wave velocities in profiles (f), (h) and (i) of Fig. 9 seem to support that the Moho depth is indeed shallower at Santo Antão and São Nicolau than below the remaining islands.

Deeper, between 13 and 15 km, most of the islands exhibit the presence of a thin shell characterized by higher velocities than the underlying mantle. We suggest these high-velocity lower-crustal bodies are the result of underplating processes, considered by some authors an integral part of intraplate volcanism in oceanic lithosphere (e.g Caress *et al.* 1995). Crustal thickening (by cumulative intrusions) and underplating have also been suggested as an important feature in Cape Verde, inclusively leading to the modification of the architecture of the archipelago's flexural moat (Ali *et al.* 2003) and being responsible for significant island uplift trends (Ramalho *et al.* 2010a,b; Ramalho 2011).

Below 14–15 km, in the uppermost mantle, we observe that the *S*-wave velocities are particularly higher beneath the northwest group and slightly higher close to the island of Santiago as also observed by Vinnik *et al.* (2012). In their study, the 1-D shear wave velocity model obtained from simultaneous inversion of combined *Ps* and *Sp* receiver functions measured in São Vicente and São Nicolau, display higher velocities between 10 and 20 km depth, than at SALA (Sal station) and SACV + MLOS (Santiago and Fogo combined) These higher velocities below the northwest of the archipelago could reflect solidified remnants of magma reservoirs, which fed the volcanism in these islands, and that are now significantly colder than in the terminus of the eastern-to-southern chain.

7 CONCLUSIONS

We imaged the 3-D *S*-wave structure of the upper 23 km below the Cape Verde archipelago based on Rayleigh-wave group velocities measured from ambient noise PCC, in a period band between 10 to 24 s. Our results show shear wave absolute velocities, varying between 2.7 to 4.6 km s^{-1} at each depth.

At crustal levels, the lowest velocities were found beneath and around the islands of Fogo and Brava. We attributed these low velocities to active volcanism and to a predominance of melt pockets or less likely to a stronger hydrothermal alteration of the crust. Descending into the upper mantle, the velocity increases quite sharply, especially beneath the northwest islands where the velocity becomes clearly higher than in the rest of the archipelago. The higher shear wave velocities in that area are interpreted as remnants of magma reservoirs, which fed the volcanism of the northwest islands. The remaining islands show velocities close to the average below ∼13 km. Shear wave velocity profiles support previous findings of a shallower Moho beneath the islands of Santo Antão and São Nicolau than beneath the other islands. Beneath all islands, with exception of Boavista, lenticular shaped high-velocity layers stand out below the crust. We speculate that these layers could be the result of crustal underplating processes that took place during hotspot volcanism.

The results presented in this study are in good agreement with previous studies, which due to the data and/or methodology limitations could not resolve the Cape Verde upper structure (crust and uppermost mantle). Ambient noise tomography is a useful technique in imaging the crust and upper-mantle features beneath oceanic islands, where other techniques (e.g. local earthquake tomography) are not suitable. However, we faced two major limitations: the uneven distribution of inter-station paths due to the island's geometry, and the effect of a water layer which made it difficult to measure unambiguously fundamental-mode dispersion velocities at frequencies above 0.1 Hz. To overcome these problems, a deployment of regularly spaced OBS would allow the improvement of the azimuthal coverage. On the other hand, cross-correlations of the horizontal components would also allow the observation of Love waves, which are not sensitive to the water layer.

ACKNOWLEDGMENTS

This study was supported by Fundação para a Ciência e a Tecnologia (FCT) project SIGHT (ref. PTDC/CTA-GEF/30264/2017) and it is also a contribution to FCT projects FIRE (ref. PTDC/GEO- GEO/1123/2014) and RESTLESS (ref. PTDC/CTA-GEF/6674/2020). This work was also supported by the Portuguese Fundação para a Ciência e a Tecnologia (FCT) I.P./MCTES through national funds (PIDDAC)—UIDB/50019/2020. JC was supported by FCT under the PhD grant PD/BD/114480/2016 and under the project PTDC/CTA-GEF/30264/2017. RSR acknowledges his former IF/01641/2015 fellowship funded by FCT. MS thanks SANIMS (RTI2018-095594-B-I00). All figures were made using GMT—Generic Mapping Tools (Wessel *et al.* 2013). Data pre-processing was done using SAC—Seismic Analysis code (Goldstein & Snoke 2005).

DATA AVAILABILITY

The data underlying this paper are available in GEOFON data centre at https://geofon.gfz-potsdam.de/doi/network/9A/2007, and can be accessed under the network code 9A.

REFERENCES

Acevedo, J., Fernández-Viejo, G., Llana-Fúnez, S., López-Fernández, C. & Olona, J., 2019. Ambient noise tomography of the southern sector of the Cantabrian Mountains, NW Spain, *Geophys. J. Int.,* **219**(1), 479–495.

Ali, M. Y., Watts, A. B. & Hill, I., 2003. A seismic reflection profile study of lithospheric flexure in the vicinity of the Cape Verde Islands, *J. geophys. Res.: Solid Earth,* **108**(B5), 1–24.

Bensen, G. D., Ritzwoller, M. H. & Shapiro, N. M., 2008. Broadband ambient noise surface wave tomography across the United States, *J. geophys. Res.: Solid Earth,* **113**(5), 1–21.

Brandmayr, E., Kuponiyi, A. P., Arroucau, P. & Vlahovic, G., 2016. Group velocity tomography of the upper crust in the eastern Tennessee seismic zone from ambient noise data, *Tectonophysics,* **688,** 148–156.

Burke, K. & Wilson, J., 1972. Is the African Plate stationary? *Nature,* **239**(5372), 387–390.

Bussat, S. & Kugler, S., 2009. Recording noise-estimating shear-wave velocities: Feasibility of offshore ambient-noise surface-wave tomography (ANSWT) on a reservoir scale., Society of Exploration Geophysics - Technical Program Expanded Abstracts 2009, 1627–1631.

Caress, D. W., McNutt, M. K., Detrick, R. S. & Mutter, J. C., 1995. Seismic imaging of hotspot-related crustal underplating beneath the Marquesas Islands, *Nature,* **373**(6515), 600–6003.

Carvalho, J., Bonadio, R., Silveira, G., Lebedev, S., Mata, J., Arroucau, P. & Celli, N. L., 2019b. Evidence for high temperature in the upper mantle beneath Cape Verde archipelago from Rayleigh-wave phase-velocity measurements, *Tectonophysics,* **770**(October), 228225.

Carvalho, J. F., Silveira, G., Schimmel, M. & Stutzmann, E., 2019a. Characterization of microseismic noise in Cape Verde, *Bull. seism. Soc. Am.,* **109**(3), 1099–1109.

Corela, C., Silveira, G., Matias, L., Schimmel, M. & Geissler, W. H., 2017. Ambient seismic noise tomography of SW Iberia integrating seafloor- and land-based data, *Tectonophysics,* **700-701,** 131–149.

Eisele, S., Freundt, A., Kutterolf, S., Ramalho, R.S., Kwasnitschka, T., Wang, K.L. & Hemming, S.R., 2015. Stratigraphy of the Pleistocene, phonolitic Cão Grande Formation on Santo Antão, Cape Verde, *J. Volc. Geotherm. Res.,* **301,** 204–220.

Dziewonski, A. M. & Anderson, D. L., 1981. Preliminary reference Earth model, *Phys. Earth planet. Inter.,* **25**(4), 297–356.

Faria, B. & Fonseca, J. F. B. D., 2014. Investigating volcanic hazard in Cape Verde Islands through geophysical monitoring: network description and first results, *Natural Hazard Earth Syst. Sci.,* **14**(2), 485–499.

Fontaine, F. R., Barruol, G., Tkalčić, H., Wölbern, I., Rümpker, G., Bodin, T. & Haugmard, M., 2015. Crustal and uppermost mantle structure variation beneath La Réunion hotspot track, *Geophys. J. Int.,* **203**(1), 107–126.

GEBCO Compilation Group, 2020 *GEBCO 2020 Grid,* doi:10.5285/a29c5465-b138-234d-e053-6c86abc040b9

Goldstein, P. & Snoke, A., 2005. SAC availability for the IRIS community, *Incorporated Research Institutions for Seismology Newsletter,* **7** (UCRL-JRNL-211140).

Gorbatikov, A. V., Montesinos, F. G., Arnoso, J., Stepanova, M. Y., Benavent, M. & Tsukanov, A. A., 2013. New features in the subsurface structure model of El Hierro Island (Canaries) from low-frequency microseismic sounding: an insight into the 2011 seismo-volcanic crisis, *Surv. Geophys.,* **34**(4), 463–489.

Grevemeyer, I., Helffrich, G., Faria, B., Booth-Rea, G., Schnabel, M. & Weinrebe, W., 2010. Seismic activity at Cadamosto seamount near Fogo Island, Cape Verdes - formation of a new ocean island? *Geophys. J. Int.,* **180**(2), 552–558.

Hable, S., Sigloch, K., Stutzmann, E., Kiselev, S. & Barruol, G., 2019. Tomography of crust and lithosphere in the western Indian Ocean from noise cross-correlations of land and ocean bottom seismometers, *Geophys. J. Int.,* **219**(2), 924–944.

Haned, A., Stutzmann, E., Schimmel, M., Kiselev, S., Davaille, A. & Yelles-Chaouche, A., 2016. Global tomography using seismic hum, *Geophys. J. Int.,* **204**(2), 1222–1236.

Hariharan, A., Dalton, C. A., Ma, Z. & Ekström, G., 2020. Evidence of Overtone Interference in Fundamental - Mode Rayleigh Wave Phase and Amplitude Measurements, *J. geophys. Res.: Solid Earth,* **125**(1), 1–17.

Helffrich, G., Faria, B., Fonseca, J. F. B. D., Lodge, A. & Kaneshima, S., 2010. Transition zone structure under a stationary hot spot: cape Verde, *Earth planet. Sci. Lett.,* **289**(1–2), 156–161.

Herrmann, R. B., 2013. Computer Programs in seismology: an evolving tool for instruction and research, *Seismol. Res. Lett.,* **84**(6), 1081–1088.

Holm, P.M., Grandvuinet, T., Friis, J., Wilson, J.R., Barker, A.K. & Plesner, S., 2008. *J. geophys. Res.: Solid Earth,* **113**(B8).

Laske, G., Masters, G., Ma, Z. & Pasyanos, M., 2013. Update on CRUST1.0—A 1-degree global model of Earth's crust, *Geophys. Res. Abstr*(Vol., **15,** p. 2658). Abstract EGU2013–2658

Le, B.M., Yang, T., Chen, Y.J. & Yao, H.,, 2018. Correction of OBS clock errors using Scholte waves retrieved from cross-correlating hydrophone recordings, *Geophys. J. Int.,* **212**(2), 891–899.

Leahy, G. M., Collins, J. A., Wolfe, C. J., Laske, G. & Solomon, S. C., 2010. Underplating of the Hawaiian Swell: evidence from teleseismic receiver functions, *Geophys. J. Int.,* **183**(1), 313–329.

Leva, C., Rümpker, G., Link, F. & anf Wölbern, I., 2019. Mantle earthquakes beneath Fogo volcano, Cape Verde: evidence for subcrustal fracturing induced by magmatic injection, *J. Volc. Geotherm. Res.,* **386,** 106672. 10.1016/j.jvolgeores.2019.106672

Liu, X. & Zhao, D., 2021. Seismic evidence for a plume-modified oceanic lithosphere–asthenosphere system beneath Cape Verde, *Geophys. J. Int.,* **225**(2), 872–886.

Lodge, A. & Helffrich, G., 2006. Depleted swell root beneath the Cape Verde Islands, *Geology,* **34**(6), 449.

Lu, Y., Stehly, L. & Paul, A., & AlpArray Working Group., 2018. High-resolution surface wave tomography of the European crust and uppermost mantle from ambient seismic noise, *Geophys. J. Int.,* **214**(2), 1136–1150.

Mata, J. *et al.*, 2017. The 2014-15 eruption and the short-term geochemical evolution of the Fogo volcano (Cape Verde): evidence for small-scale mantle heterogeneity, *Lithos,* **288-289,** 91–107.

Matos, C., Silveira, G., Matias, L., Caldeira, R., Ribeiro, M. L., Dias, N. A. & Bento dos Santos, T., 2015. Upper crustal structure of Madeira Island revealed from ambient noise tomography, *J. Volc. Geotherm. Res.,* **298**(June), 136–145.

McNutt, M., 1988. Thermal and mechanical properties of the Cape Verde Rise, *J. geophys. Res. (Solid Earth),* **93**(B4), 2784–2794.

Moschetti, M. P., Ritzwoller, M. H. & Shapiro, N. M., 2007. Surface wave tomography of the western United States from ambient seismic noise: rayleigh wave group velocity maps, *Geochem. Geophys. Geosyst.,* **8**(8), 1–10.

Müller, R. D., Sdrolias, M., Gaina, C. & Roest, W. R., 2008. Age, spreading rates, and spreading asymmetry of the world's ocean crust, *Geochem. Geophys. Geosyst.,* **9**(4),.

Nettles, M. & Dziewonski, A. M., 2011. Effect of higher-mode interference on measurements and models of fundamental-mode surface-wave dispersion, *Bull. seism. Soc. Am.,* **101**(5), 2270–2280.

Nishida, K., Montagner, J. P. & Kawakatsu, H., 2009. Global surface wave tomography using seismic hum, *Science,* **326**(5949), 112.

Nuñez, E., Schimmel, M., Stich, D. & Iglesias, A., 2019. Crustal velocity anomalies in Costa Rica from ambient noise tomography, *Pure appl. Geophys.,* doi:10.1007/s00024-019-02315z

Picozzi, M., Parolai, S., Bindi, D. & Strollo, A., 2009. Characterization of shallow geology by high-frequency seismic noise tomography, *Geophys. J. Int.,* **176**(1), 164–174.

Pim, J., Peirce, C., Watts, A. B., Grevemeyer, I. & Krabbenhoeft, A., 2008. Crustal structure and origin of the Cape Verde Rise, *Earth planet. Sci. Lett.,* **272**(1–2), 422–428.

Pinzon, J. I., Silveira, G. M., Custodio, S., Matias, L. M., Krueger, F., Dahm, T. & Carvalho, J., 2019. How are ambient noise dispersion curves recorded in OBSs affected by the water?, In *AGU Fall Meeting Abstracts,* Vol., **2019,** pp. S23C–0649.

Pollitz, F., 1991. Two-stage model of African absolute motion during the last 30 million years, *Tectonophysics,* **194**(1–2), 91–106.

Poveda, E., Julià, J., Schimmel, M. & Perez-Garcia, N., 2018. Upper and middle crustal velocity structure of the Colombian Andes from ambient noise Tomography: investigating subduction-related magmatism in the overriding plate, *J. geophys. Res.: Solid Earth,* **123**(2), 1459–1485.

Pranata, B., Yudistira, T., Widiyantoro, S., Brahmantyo, B., Cummins, P. R., Saygin, E. & Cipta, A., 2019. Shear wave velocity structure beneath Bandung basin, West Java, Indonesia from ambient noise tomography, *Geophys. J. Int.,* 1045–1054, doi:10.1093/gji/ggz493

Ramalho, R., Helffrich, G., Cosca, M., Vance, D., Hoffmann, D. & Schmidt, D.N., 2010a. Episodic hotspot swell growth inferred from variable uplift from the Cape Verde hot spot Islands, *Nat. Geosci.,* **3,** 774–777.

Ramalho, R., Helffrich, G., Cosca, M., Vance, D., Hoffmann, D. & Schmidt, D.N., 2010b. Vertical movements of ocean island volcanoes: insights from a stationary plate, *Mar. Geol.,* **275,** 84–95.

Ramalho, R. A., 2011. Building the Cape Verde islands, in *Springer Theses,* doi:10.1007/978-3-642-19103-9

Rawlinson, Nicholas & Sambridge, M., 2005. The fast marching method: an effective tool for tomographic imaging and tracking multiple phases in complex layered media, *Explor. Geophys.,* **36**(4), 341–350.

Rawlinson, N., Reading, A. M. & Kennett, B. L., 2006. Lithospheric structure of Tasmania from a novel form of teleseismic tomography, *J. geophys. Res.: Solid Earth,* **111**(B2).

Romanowicz, B., 2002. Inversion of surface waves: a review, *Int. Geophys. Ser.,* **81(A),** 149–174.

Saygin, E. & Kennett, B. L. N., 2012. Crustal structure of Australia from ambient seismic noise tomography, *J. geophys. Res.: Solid Earth,* **117**(1), 1–15.

Samrock, L.K., Wartho, J.A. & Hansteen, T.H., 2019. ^{40}Ar-^{39}Ar geochronology of the active phonolitic Cadamosto Seamount, Cape Verde, *Lithos,* **344,** 464–481.

Schlaphorst, D. *et al.*, 2021. Variation in upper plate crustal and lithospheric mantle structure in the greater and Lesser Antilles from ambient noise tomography, *Geochem. Geophys. Geosyst.,* **22**(7), e2021GC009800.

Schimmel, Martin., 1999. Phase cross-correlations: design, comparisons, and applications, *Bull. seism. Soc. Am.,* **89**(5), 1366–1378.

Schimmel, M. & Gallart, J., 2007. Frequency-dependent phase coherence for noise suppression in seismic array data, *J. geophys. Res.: Solid Earth,* **112**(B4), 1–14.

Schimmel, M., Stutzmann, E. & Gallart, J., 2011. Using instantaneous phase coherence for signal extraction from ambient noise data at a local to a global scale, *Geophys. J. Int.,* **184**(1), 494–506.

Schimmel, Martin, Stutzmann, E. & Ventosa, S., 2017. Measuring group velocity in seismic noise correlation studies based on phase coherence and resampling strategies, *IEEE Trans. Geosci. Remote Sens.,* **55**(4), 1928–1935.

Silveira, G., Dias, N., Kiselev, S., Stutzmann, E., Custódio, S. & Schimmel, M., 2022. Imaging the crust and uppermost mantle structure of Portugal (West Iberia) with seismic ambient noise, *Geophys. J. Int.,* **230**(2) 1106–1120.

Shapiro, N. M., Campillo, M., Stehly, L. & Ritzwoller, M. H., 2005. High-resolution surface-wave tomography from ambient seismic noise, *Science,* **307**(5715), 1615–1618.

Sleep, N. H., 1990. Hotspots and mantle plumes: some phenomenology, *J. geophys. Res.: Solid Earth,* **95**(B5), 6715–6736.

Stockwell, R. G., Mansinha, L. & Lowe, R. P., 1996. Localization of the complex spectrum: the S transform, *IEEE Trans. Signal Process.,* **44**(4), 998–1001.

Stork, A.L., Allman, C., Curtis, A., Kendall, J.M. & White, D.J., 2018. Assessing the potential to use repeated ambient noise seismic tomography to detect CO2 leaks: application to the Aquistore storage site, *Int. J. Greenhouse Gas Control,* **71,** 20–35.

Stutzmann, E. & Montagner, J. P., 1993. An inverse technique for retrieving higher mode phase velocity and mantle structure, *Geophys. J. Int.,* **113**(3), 669–683.

Torres, P., Silva, L., Munhá, J., Caldeira, R., Mata, J. & Tassinari, C. C., 2010. Petrology and geochemistry of lavas from Sal Island: implications for the variability of the Cape Verde magmatism, *Comun. Geol.,* **97,** 35–62.

Vales, D., Dias, N. A., Rio, I., Matias, L., Silveira, G., Madeira, J. & Haberland, C., 2014. Intraplate seismicity across the Cape Verde swell: a contribution from a temporary seismic network, *Tectonophysics,* **636,** 325–337.

Vinnik, L., Silveira, G., Kiselev, S., Farra, V., Weber, M. & Stutzmann, E., 2012. Cape Verde hotspot from the upper crust to the top of the lower mantle, *Earth planet. Sci. Lett.,* **319-320,** 259–268.

Wang, Y., Lin, F.C., Schmandt, B. & Farrell, J., 2017. Ambient noise tomography across Mount St. Helens using a dense seismic array, *J. geophys. Res.,* **122,** 4492–4508.

Weber, M., Silveira, G. & Schulze, A., 2007: The COBO/CV-PLUME temporary seismic network, GFZ Data Services. Other/Seismic Network. doi:10.14470/4N7552467332.

Wessel, P., Smith, W. H., Scharroo, R., Luis, J. & Wobbe, F., 2013. Generic Mapping Tools: improved version released, *Eos Trans. Am. geophys. Un.,* **94**(45), 409–410.

Williams, C. A., Hill, I. A., Young, R. & White, R. S., 1990. Fracture zones across the Cape Verde rise, NE Atlantic, *J. geol. Soc.,* **147**(5), 851–857.

Wilson, D. J., Peirce, C., Watts, A. B., Grevemeyer, I. & Krabbenhoeft, A., 2010. Uplift at lithospheric swells—I: seismic and gravity constraints on the crust and uppermost mantle structure of the Cape Verde mid-plate swell, *Geophys. J. Int.,* **182**(2), 531–550.

Wilson, D. J., Peirce, C., Watts, A. B. & Grevemeyer, I., 2013. Uplift at lithospheric swells—II: is the Cape Verde mid-plate swell supported by a lithosphere of varying mechanical strength?, *Geophys. J. Int.,* **193**(2), 798–819.

Yang, Y., Ritzwoller, M. H., Levshin, A. L. & Shapiro, N. M., 2007. Ambient noise Rayleigh wave tomography across Europe, *Geophys. J. Int.,* **168**(1), 259–274.

SUPPORTING INFORMATION

Supplementary data are available at *GJI* online.

Figure S1.1: Example of dispersion measurements obtained for different inter-station paths. Top panel: amplitude spectra; middle panel: energy diagram and bottom panel: automatically selected dispersion measurements. These examples show the difficulties found in properly selecting the measurements at frequencies higher than 0.1 Hz due to the existence of multiple signals (marked by white circles), thus it is not possible to continuous follow the fundamental-mode group velocity with confidence.

Figure S1.2: Measurement of PCC stacks and group velocities for station pair CVBV1–CVSA4, separated by 270 km. PCC stack for the wide frequency band (0.03–0.5 Hz) and the corresponding group velocities estimated for the wide band can be observed on Fig. 3. PCC stacks for the bands of 0.03–0.1, 0.1–0.2 and 0.2–0.5 Hz are represented in the top panel with the corresponding group velocities estimated below.

Figure S2.1: Comparison between Rayleigh-wave synthetics for the fundamental mode (coloured lines) and real data group-velocities measurements (black lines). The different coloured lines represent different paths: Path1–yellow; Path 2–blue; Path 3–red; Path 4–green and Path 5–pink.

Figure S2.2: Synthetic group velocities of Rayleigh-wave fundamental mode (black dots) and first two overtones (blue and red dots), considering different water layer thickness. Each plot on the left (A, B and C) correspond to an inter-island path (A, B and C) on the map (on the right).

Figure S2.3: Synthetic seismograms. In each panel, left and right, we show all modes added together (black), the fundamental mode (red) and first higher mode (green). Second overtone is not represented because it has a negligible amplitude. *X*-axis represents time (s) and *Y*-axis corresponds to the frequency (Hz).

Figure S.2.4: Energy diagram of the time-series (black line in Fig. S2.3, Supporting Information) evincing the complexity of the signals at short periods (higher frequencies).

Figure S3: Checkerboard test using the FMST method (Rawlinson & Sambridge 2005) for different space grids for 17 s. Top: input model. Bottom: recovered anomalies—(a) and (b) represent the output with a smaller grid size and (c) corresponds to the output anomalies of the chosen checkerboard (Fig. 6 of the manuscript). Smaller grid sizes exhibit smearing, specially where there are no crossing paths.

Figure S4: Trade-off curves for the Rayleigh-wave group-velocity inversion at 18 s. (a) Data misfit with model roughness for damping factor $\varepsilon = 5$. (b) Data misfit with model variance for smoothing factor $\eta = 50$. (c) Data misfit as function of number of iterations for damping and smoothing previously selected ($\varepsilon = 5$ and $\eta = 50$).

Figure S5: Group-velocity maps for some of the considered periods (10–21 s). Slower and faster than average velocities are represented with warmer and cooler colours, respectively.

Figure S6: Left: *S*-wave velocity model used for computing the depth sensitivity kernels of group velocity versus shear wave velocity (Lodge & Helffrich 2006). Right: depth sensitivity kernels of fundamental-mode Rayleigh wave group velocity to shear wave velocity for periods of 10, 15 and 20 s.

Table S1: Land and oceanic block dimensions considered to calculate Rayleigh-wave synthetic group velocities, aiming to reproduce three chosen inter-island paths, one oceanic path, and one land path.

Please note: Oxford University Press is not responsible for the content or functionality of any supporting materials supplied by the authors. Any queries (other than missing material) should be directed to the corresponding author for the article.